International Journal of Heat and Mass Transfer 51 (2008) 6219–6234

Contents lists available at ScienceDirect

International Journal of Heat and Mass Transfer

journal homepage: www.elsevier.com/locate/ijhmt

DNS of rotating buoyancy– and surface tension–driven flow

A. Raufeisen [a,b,*], M. Breuer [a], T. Botsch [b], A. Delgado [a]

[a] Lehrstuhl für Strömungsmechanik, Friedrich-Alexander-Universität Erlangen-Nürnberg, Cauerstraße 4, D-91058 Erlangen, Germany
[b] Fakultät Verfahrenstechnik, Georg-Simon-Ohm-Hochschule Nürnberg, Wassertorstraße 10, D-90489 Nürnberg, Germany

ARTICLE INFO

Article history:
Received 23 April 2007
Received in revised form 12 November 2007
Available online 2 July 2008

Keywords:
Crystal growth
Czochralski
Direct numerical simulation
Large-eddy simulation
Buoyancy
Surface tension
Rotation
Rayleigh–Bénard–Marangoni convection

ABSTRACT

The combination of turbulent buoyant flow with a free surface (Rayleigh–Bénard–Marangoni convection) and rotation is hardly investigated in detail, especially for low Prandtl number fluids, although it can be found in several applications such as Czochralski (Cz) crystal growth. Therefore, a Direct Numerical Simulation (DNS) of such a Cz case with an idealized cylindrical crucible geometry of 170 mm radius and a rotating crystal of 50 mm radius was conducted applying realistic boundary conditions, which lead to the dimensionless numbers of $Re = 4.7 \times 10^4$, $Gr = 2.2 \times 10^9$, $Ma = 2.8 \times 10^4$, and $Ra = 2.8 \times 10^7$. The computational grid contained ca. 8.4 million control volumes to resolve all turbulent scales based on a finite-volume scheme for curvilinear block-structured grids and an explicit time discretization. The resulting velocity and temperature fields show fully developed three-dimensional turbulence and are characterized by thermal buoyant plumes rising from the bottom of the crucible to the free surface, surface tension effects, and the strong impact of the counterrotating crystal. The analysis of the instantaneous flow revealed that in the rotating melt a large, slowly moving spiral vortex evolves. The averaged data show the formation of Bénard cell-like structures. Below the crystal, along the free surface, and especially at the corner of the crystal, the turbulence intensity is strongest. The DNS results were generated and analyzed in detail in order to serve as a reference and will also be made available to the public for further investigations. Within an ongoing study these data will be used to validate computations for practical applications employing the Large-Eddy Simulation (LES) technique, which is used to model the turbulent flow and temperature field in order to save computational time compared to DNS.

1. Introduction

Flows dominated by buoyancy and surface tension effects are among the most common flow phenomena including heat transfer occurring in nature. Therefore, numerous investigations have been conducted in this field. The first observations of pattern formation in an open liquid heated from below were reported by Bénard in 1900 [1,2]. Lord Rayleigh published a theoretical analysis of a slightly different and simpler configuration, where the liquid is confined between two plates, in 1912 [3]. This system is nowadays called after Rayleigh and Bénard (R–B), although there is no free surface like in the original experiment by Bénard. It is still subject of research activities, because many properties of flow and heat transfer, especially in the turbulent or transitional state, can be determined [4,5]. In the last decades, besides experiments and theoretical considerations, numerical simulations have become more important, because they can provide more detailed data such as fully three-dimensional time-dependent velocity and temperature fields. Furthermore, a broader range of parameters can be examined more quickly and easily, e.g. in case of low Prandtl numbers. Even physically infeasible, but scientifically interesting studies like on the effect of zero Prandtl number [6], can be conducted via simulations. On one side, the mechanisms of pattern formation and instabilities were analyzed, see [7–10] for an extensive description. Depending on the governing parameters, stationary or oscillating, symmetric or asymmetric hexagonal, square, and roll patterns as well as traveling waves among others were found. However, for high values of the characteristic dimensionless numbers, the flow structure becomes chaotic in nature, i.e. turbulent. On the other side, attempts were made to find scaling laws for turbulent flow and heat transfer (especially between important dimensionless parameters such as *Ra*, *Pr*, and *Nu*), see [11,12] for an overview. Despite the large number of studies, no agreement has been found yet upon a unique dependence, especially in the regions of extreme values, i.e. very large Rayleigh numbers ($Ra > 10^{15}$) [13–16] and/or low Prandtl numbers [6,17–27]. The latter case is especially important for applications involving liquid metals or metalloids, as for example in casting or crystal growth of semiconductors.

The original case of Bénard [1,2] including a free surface is less studied, although at least of the same scientific and practical importance. The fact that the pattern formation is caused by

* Corresponding author. Address: Fakultät Verfahrenstechnik, Georg-Simon-Ohm-Hochschule Nürnberg, Wassertorstraße 10, D-90489 Nürnberg, Germany. Tel.: +49 911 5880 1198; fax: +49 911 5880 5475.
E-mail address: alexander.raufeisen@ohm-hochschule.de (A. Raufeisen).

0017-9310/$ - see front matter © 2008 Elsevier Ltd. All rights reserved.
doi:10.1016/j.ijheatmasstransfer.2008.01.041

Nomenclature

Abbreviations

B–M	Bénard–Marangoni
CV	control volume
Cz	Czochralski
DNS	direct numerical simulation
LES	large-eddy simulation
R–B	Rayleigh–Bénard

Greek symbols

β	thermal expansion coefficient
λ_v	viscous sublayer thickness
μ	dynamic viscosity
ν	kinematic viscosity
ω	angular velocity
ρ	density
σ	surface tension
σ_{SB}	Stefan–Boltzmann constant
ε	emissivity
ε_k	dissipation rate

Latin symbols

c_p	specific heat capacity
G	buoyancy term
g	gravitational acceleration
H, h	height
k	thermal conductivity
k	turbulent kinetic energy
P	pressure
P	production term
R, r	radius
R_1, R_2	curvature radii
T	temperature
t	time
u_i	velocities
x_i	coordinate direction

Subscripts

b	buoyancy
c	crucible
n, s, t	normal and tangential directions
s	crystal

Superscripts

$()^+$	dimensionless wall-distance
$\langle\rangle$	time-average

thermocapillary forces was ignored by Bénard himself, and first discovered by Block [28]. Due to the combination of these two effects (buoyancy and thermocapillary convection), the phenomenon is mostly called Bénard–Marangoni (B–M) convection. The first stability analysis by Pearson [29] neglected the buoyancy effect, which was then included in the work by Nield [30]. Like in R–B convection, mostly the instabilities and dependencies of *Nu*, *Ra*, and *Pr* are studied in the literature (see [31,32], e.g.). Again, the low-Prandtl number regime is of special interest due to its relevance for crystal growth applications. The flow structure changes significantly with decreasing *Pr*, e.g. the hexagonal cells become inverted [33]. Furthermore, so-called inertial convection [34] occurs, i.e. the kinetic energy of the moving fluid is much larger than the dissipated energy, analog to a mechanical flywheel. A detailed literature overview can be found in [35,36]. In B–M convection, shear stresses can occur at the free surface which are induced by the movement of the surrounding gas. However, in most cases they can be neglected and the so-called one-layer approach can be used, see the analysis in [37]. Furthermore, stresses are caused by the deformation of the free surface and lead to long-wavelength instabilities, but they are restricted to certain parameters like large aspect ratios and thus are of marginal importance for typical configurations. B–M convection is also investigated in combination with other physical effects like rotation (see [24,38–40], e.g.), which changes the flow patterns due to the additional Coriolis and centrifugal forces. Also magnetic fields in case of electrically conducting fluids (see [41], e.g.) are used to influence the velocity field.

All effects described can be found in Czochralski (Cz) systems for crystal growth of semiconductors such as silicon with a Prandtl number of about 0.01. With this method, more than 90% of the silicon single crystals for the electronics industry are grown. The process has a simple setup: The molten silicon is contained in an open crucible, which is rotating and heated from the side. Starting with a seed crystal, the bulk crystal is slowly pulled from the melt, while rotating in the opposite direction of the crucible. Due to this configuration, the above mentioned different forces act on the melt: coriolis and centrifugal forces, buoyancy, and surface tension, leading to a complex flow similar to rotating Bénard–Marangoni convection in combination with a rotating disc (for the crystal). Comprehensive theoretical studies on the flow structure and instabilities in Cz melts based on experimental observations were conducted by Ristorcelli and Lumley [42], Müller [43], and Kakimoto [44], who also compared the results with numerical simulations. Not less than 10 different types of instability mechanisms were found. Also Cz-specific pattern formations were observed, such as spoke patterns [45] and cellular structures [46].

However, experimental measurements in Cz systems are problematic, because of the very hot and chemically aggressive melt, which complicates the use of thermocouples for temperature measurement. Furthermore, the opaqueness of the melt hampers optical measurement techniques. Therefore, only very few experimental data are available from literature, e.g. from Jones [47], who used a transparent model fluid, or Tanaka et al. [48], employing a CCD camera for observation of the surface temperature. Later, also X-ray radiography [49], and highly insulated thermocouples [43,50] were used. All these techniques have limitations according to their nature. With the latter method, e.g., only a few discrete points can be measured, the inserted thermocouple disturbs the flow structure, and the extra insulations dampen the high-frequency signals.

Thus, to obtain more detailed data, "numerical experiments" have become quite popular. In early computations, many simplifications were applied due to the limited computing resources, such as the assumption of 2D axisymmetry. However, the flow is three-dimensional, time-dependent, and, caused by the increasing size of the crucible and the resulting high Reynolds and Rayleigh numbers, fully turbulent [51]. This makes computer simulations difficult, as the flow field has to be resolved very finely, if an accurate solution is desired. Such Direct Numerical Simulations (DNS), which resolve all turbulent scales, are therefore very expensive and time-consuming, so that only a few cases are known from literature (see Table 1).

The first three-dimensional computation was conducted by Mihelčić in 1984 [52], but with a very coarse grid not adequate for DNS. A reasonable (but still insufficient) resolution in terms of number of CVs was employed by Xiao and Derby [53] for oxide melts. En-

Table 1
Overview of simulations carried out for Cz crystal growth using DNS and Quasi-DNS

Reference	Year	Gr	Ta	R_c	CVs
Tanaka et al. [48][a]	1997	1.6×10^{9} [c]	$2.6 \times 10^{6} - 2.86 \times 10^{9}$	220 mm	326,106
Kishida and Okazawa [61]	1999				
Kishida et al. [62]	2005	1.08×10^{9} [c]	$4.2 \times 10^{9} - 3.4 \times 10^{11}$	220 mm	312,000
Enger [51] [a]	2001	5×10^{8} [b]	$1.6 \times 10^{9} - 10^{10}$	170 mm	4,980,736
Enger et al. [54] [a]	2001	5×10^{8} [b]	$1.6 \times 10^{9} - 10^{10}$	170 mm	1,945,600
Basu et al. [46] [a]	2000	1.6×10^{9} [b]	2.86×10^{9}	220 mm	336,960
Kumar et al. [60]	2003	1.6×10^{9} [b]	2.86×10^{9}	220 mm	336,960
Kumar et al. [55]	2003	5×10^{8} [b]	1.6×10^{9}	170 mm	1,000,000
Schäfer et al. [56]	2005	5×10^{8} [b]	1.6×10^{9}	170 mm	1,000,000
Vizman et al. [59]	2001	3×10^{9} [c]	$1.6 \times 10^{9} - 10^{10}$	170 mm	950,000
Wagner [64]	2003,				
Wagner and Friedrich [65]	2004	1.6×10^{9} [c]	10^{10}	170 mm	2,840,064
Watanabe et al. [63]	2006	2×10^{10} [c]	–	320 mm	330,000

[a] Without Marangoni convection.
[b] Based on crucible height.
[c] Based on crucible radius.

ger et al. [54] and Enger [51] were the first who computed a large industrial Cz crucible with 170 mm radius with a fine grid, obtaining very detailed results, but neglegting the Marangoni effect. However, this has a major influence on the flow structure in the silicon melt, as Kumar et al. [55] found out by repeating the simulations including surface tension. The same configuration was also used for a detailed three-dimensional visualization and computational steering of the Cz melt flow [56]. Also oxide melts were analyzed [57,58], simulating the experiments by Jones [47] with a model fluid in a crucible of 170 mm radius, but using less resolution, calling this method Quasi-DNS. Vizman et al. [59] computed a realistic Cz configuration similar to that in [54], but the applied resolution of approximately 950,000 cells can be estimated as too coarse for DNS. The same applies to other simulations found in the literature, such as Tanaka et al. [48], Basu et al. [46], Kumar et al. [60], Kishida and Okazawa [61] and Kishida et al. [62] and Watanabe et al. [63]. All these predictions were conducted with even less CVs (around 330,000), although the crucibles were bigger. To the authors' knowledge, the only well-resolved Cz–DNS besides Enger's was conducted by Wagner [64] and Wagner and Friedrich [65], who used an idealized cylindrical crucible geometry with computational grids of 2–4.5 million cells, simulating the idealized Cz system with different parameters for rotation and comparing the predictions to experimental results. However, the published data are not very detailed and only usable for qualitative analysis, which was done by the authors recently [66,67]. Moreover, the use of some of the parameters like material properties (e.g. thermal conductivity) and boundary conditions (e.g. the approximation of thermal radiation at the free surface by fixed heat fluxes) were not convincing. Finally, the data sets were not made available by the authors for further investigation. Consequently, no DNS data set is available, which takes all issues mentioned above into account. Thus, in the present work a new DNS was conducted for detailed analysis of the flow structure of a Cz-system and to obtain reference data for the validation of LES predictions used for turbulence modeling in practical applications.

The paper is organized as follows: Section 2 starts with the statement of the physical problem. In Section 3, the numerical method is described, and the succeeding section delivers all details of the computational grid applied. The specification of the simulation carried out can be found in Section 5. In Section 6, the results of the DNS are presented and discussed. In Section 7, the results are summarized and conclusions are drawn.

2. Problem description

For the simulations, an idealized geometry was adopted from an industrial crucible (Leybold EKZ 1300) for the growth of 100 mm silicon crystals (see Fig. 1). Both the original and modified geometry has been used many times for simulations and experiments and can be called a standard case. The crucible is assumed to be of cylindrical shape with a diameter of 340 mm, a height of 85 mm, and a 100 mm crystal on top of the melt, which is not explicitly simulated, but treated as a boundary condition. Details about the boundary conditions can be found in Section 3.3. The melt-crystal interface is assumed to be flat. The crucible is rotating with $\omega_c = 5$ rpm in counter-clockwise direction, while the crystal is counterrotating with $\omega_s = -20$ rpm. The crucible is heated from the side, which is modeled via a fixed temperature distribution at the side walls $T(z)$ and the bottom of the crucible $T(r)$. These data were interpolated from an experiment conducted by Gräbner et al. [50]. Thermal radiation loss is considered from the free surface of the melt to the surrounding atmosphere ($T_{env} = 1600$ K). Additionally, at the free surface, Marangoni convection is accounted for by assuming a temperature-dependent surface tension $\sigma(T)$. The material properties of the silicon melt are given in Table 2.

The characteristic scales of the process are the crucible radius $R_c = 170$ mm and the maximum temperature difference $\Delta T = 37.8$ K, derived from the maximum temperature at the crucible $T_{max} = 1722.8$ K, located at the corner between bottom and sidewall, and the melting temperature of silicon (at the crystal) $T_{min} = T_{melt} = 1685$ K, from which also a characteristic buoyant velocity $u_b = \sqrt{\beta g R_c \Delta T} = 0.094$ m/s can be calculated. From these reference quantities together with the material data, the relevant dimensionless numbers of the Cz system can be determined, see Table 2. The dimensionless temperature is defined as $(T - T_0)/\Delta T$ with $T_0 = (T_{max} + T_{min})/2 = 1703.9$ K, and the time scale as $R_c/u_b = 1.81$ s.

The Prandtl number *Pr* of silicon is quite small, which means that the momentum diffusion is much smaller than the thermal diffusion. The convective effects are characterized by the Reynolds number *Re*, which is the quotient of convective transport and movement due to molecular momentum transport, the Grashof number *Gr*, which states the ratio of buoyant to viscous forces, and the Rayleigh number *Ra*, which is the product of *Gr* and *Pr*, and thus is two orders of magnitude smaller than *Gr*. The Rayleigh number describes the ratio of convective to diffusive transport. As it is of the order of 10^7, convection is dominant in this configuration of flow and heat transfer. Furthermore, by definition of Ristorcelli and Lumley [42], e.g., for R–B systems, the present configuration is situated close to the transition of "soft" to "hard" turbulence ($Ra_{crit} = 4 \times 10^7$). The Marangoni number *Ma* describes the ratio between surface-tension induced velocities and those due to thermal molecular transport. The magnitude of *Ma* suggests that the surface tension forces have a major influence on the flow field. Additionally, the effect of rotation is characterized by the Taylor number *Ta*, which denotes the ratio of Coriolis to viscous forces.

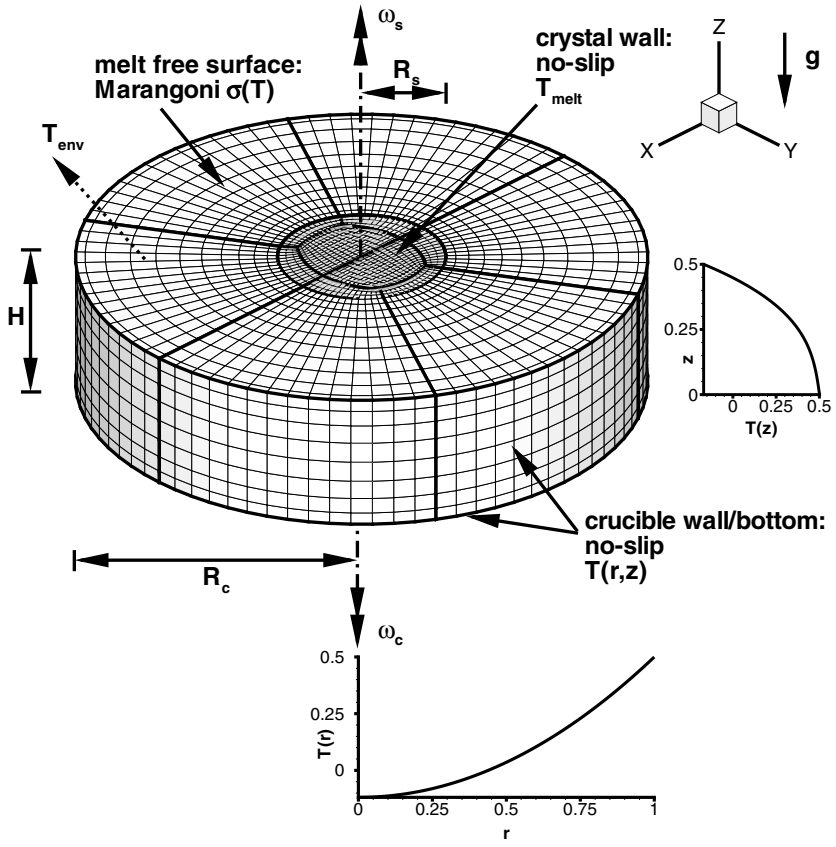

Fig. 1. Geometry and boundary conditions of the simulation and computational grid consisting of 8 blocks in O-grid configuration. Here, only every 8th grid line is shown in each direction for better visibility.

Table 2
Properties of silicon melt and resulting dimensionless numbers of the Cz simulation

Property/number	Symbol	Formula	Value	Unit
Density	ρ		2530	kg/m^3
Dynamic viscosity	μ		8.6×10^{-4}	kg/(m s)
Kinematic viscosity	ν		3.4×10^{-7}	m^2/s
Thermal expansion coefficient	β		1.4×10^{-4}	1/K
Thermal conductivity	k		67.0	J/(s m K)
Specific heat capacity	c_p		1000	J/(kg K)
Temperature coefficient of surface tension	$d\sigma/dT$		-1.0×10^{-4}	N/(m K)
Melting temperature	T_{melt}		1685	K
Emissivity	ε		0.3	
Stefan–Boltzmann constant	σ_{SB}		5.67032×10^{-8}	W/(m^2 K^4)
Surrounding temperature	T_{env}		1600	K
Prandtl	Pr	$\frac{\mu c_p}{k}$	1.284×10^{-2}	
Reynolds	Re	$\frac{R_c u_b}{\nu}$	4.697×10^4	
Reynolds (rotational)	Re_ω	$\frac{R_c^2 \omega_c}{\nu}$	4.451×10^4	
Grashof (thermal)	Gr	$\frac{\beta g R_c^3 \Delta T}{\nu^2}$	2.206×10^9	
Marangoni	Ma	$-\frac{d\sigma}{dT}\frac{R_c c_p \Delta T}{\nu k}$	2.822×10^4	
Rayleigh	Ra	$Gr\,Pr$	2.833×10^7	
Taylor	Ta	$4Re_\omega^2$	7.923×10^9	

3. Numerical formulation

3.1. Governing equations

The flow and heat transfer in the melt are governed by the three-dimensional Navier–Stokes equations for an incompressible Newtonian fluid expressing the conservation of mass, momentum and energy. Using the above mentioned characteristic scales and the resulting dimensionless numbers, the equations are non-dimensionalized. Buoyancy is taken into account by the Boussinesq approximation assuming only small temperature gradients. The simulations are conducted in a rotating frame of reference with the crucible as the reference system. Due to Coriolis and centrifugal forces induced by rotation, additional source terms must be added to the right side of the momentum equation. The viscous dissipation in the energy equation is neglected. For details see [55,60], e.g.

3.2. Finite-volume method

The computer code $\mathcal{LESOCC}$ [68–71] is used for integrating the governing equations in space and time. It is based on a three-dimensional finite-volume method for arbitrary non-orthogonal and block-structured grids. All viscous fluxes are approximated by central differences of second-order accuracy, which fits the elliptic nature of the viscous effects. The non-linear convective fluxes in the momentum equation are discretized by a central scheme of second-order accuracy (CDS-2). Although this approximation is formally only of first-order accuracy on non-uniform grids, the truncation error of the CDS is almost one order smaller than of first-order schemes due to the high quality of the grid expressed by a stretching factor close to unity [72]. Thus the discretization used here is approximately second-order accurate can be assumed appropriate for DNS computations.

Time advancement is performed by a predictor–corrector scheme. A low-storage multi-stage Runge–Kutta method (three sub-steps, second-order accuracy) is applied for integrating the momentum equations in the predictor step. Within the corrector step the Poisson equation for the pressure correction is solved implicitly by the incomplete LU decomposition method of Stone [73]. Based on the predicted pressure correction, the pressure and velocities are updated until mass

conservation is achieved. Explicit time marching works well for DNS with small time steps which are necessary to resolve turbulent motion in time. The pressure and velocity fields on a non-staggered grid are coupled by the momentum interpolation technique of Rhie and Chow [74]. A variety of different test cases (see [68–71], e.g.) served for the purpose of code validation.

The algorithm is highly vectorized and additionally parallelized by domain decomposition with explicit message-passing based on MPI (Message Passing Interface) allowing efficient computations especially on vector-parallel machines and SMP (Symmetric Multi-Processing) clusters. The present DNS predictions were carried out on the vector-parallel supercomputer NEC SX-8 at the HLRS in Stuttgart using 8 processors, i.e. 1 node.

3.3. Boundary conditions

As mentioned above, the simulations are conducted in a rotating frame of reference with the crucible as the reference system. Thus, formally the crucible is at rest, while the crystal is rotating in clockwise direction with $|\omega_c| + |\omega_s| = 25$ rpm. The angular velocity of the crucible is added to the flow field afterwards. At the crucible walls and the crystal, the no-slip condition is applied, whereas at the free surface of the melt, Marangoni convection is considered. Marangoni convection is induced by temperature gradients at the free surface of the liquid which causes changes in the surface tension and thus gives rise to fluid motion. This motion is modeled by the Laplace–Young equation, stating force balances along the surface in normal

$$-2\mu\frac{\partial u_n}{\partial x_n} = \Delta P + \sigma\left(\frac{1}{R_1}+\frac{1}{R_2}\right) \tag{1}$$

and tangential directions

$$\mu\left(\frac{\partial u_s}{\partial x_n}+\frac{\partial u_n}{\partial x_s}\right) = \frac{\partial \sigma}{\partial x_s} \quad \text{and} \quad \mu\left(\frac{\partial u_t}{\partial x_n}+\frac{\partial u_n}{\partial x_t}\right) = \frac{\partial \sigma}{\partial x_t}. \tag{2}$$

For simplicity, the free surface is assumed to be flat, i.e. the velocity in normal direction is assumed to be zero $u_n = 0$, and the curvature radii are infinite. Moreover, for low viscosities μ, the normal component of the stress $-2\mu\partial u_n/\partial x_n$ can be neglected, such that from Eq. (1) ΔP is zero. The surface tension is assumed to be a function of temperature only, which is approximated linearly by

$$\sigma = \sigma_0 + \frac{d\sigma}{dT}(T - T_0) \tag{3}$$

with a constant coefficient of proportionality $d\sigma/dT$ (see Table 2). Thermal radiation from the free surface of the melt is considered by the Stefan–Boltzmann equation:

$$k\nabla T = \sigma_{SB}\varepsilon(T^4 - T_{env}^4). \tag{4}$$

The temperature at the crucible is fixed to a certain profile, which was derived from experimental data of Gräbner et al. [50] and interpolated to the cylindrical geometry. In dimensionless form, the temperature distributions at the sidewalls and at the bottom read

$$\frac{T(z)-T_0}{\Delta T} = 4.6\left(\frac{H-z}{R_c}\right)^3 - 6.85\left(\frac{H-z}{R_c}\right)^2 + 3.615\frac{H-z}{R_c} - 0.169, \tag{5}$$

$$\text{and} \quad \frac{T(r)-T_0}{\Delta T} = 0.619\left(\frac{r}{R_c}\right)^2 - 0.119, \tag{6}$$

respectively. The profiles are depicted in Fig. 1.

4. Computational grids

4.1. Resolution requirements

For the accuracy of the simulations, the quality and resolution of the computational grids are crucial. In DNS calculations, all turbulent scales have to be resolved. Two issues have to be taken into account for this purpose. First, the resolution in the inner computational domain has to be checked, and second, the resolution of the boundary layers near solid walls has to be investigated. For the first issue a homogeneous isotropic flow field is typically assumed which allows to estimate the smallest turbulent scales. An estimation of the size of the smallest scales was first done by Kolmogorov [75,76], determining a characteristic length scale l_c for the smallest turbulent structures from the kinematic viscosity ν and the dissipation rate ε_k of the turbulent kinetic energy. With the normalization used here, the criterion reads in dimensionless form

$$l_c = \left(\frac{1}{\varepsilon_k Re^3}\right)^{\frac{1}{4}}, \tag{7}$$

where ε_k is defined as the trace of the dissipation tensor ε_{ij} in non-dimensional form and averaged in time:

$$\varepsilon_{ij} = \frac{1}{Re}\left\langle \frac{\partial u_j'}{\partial x_i}\frac{\partial u_j'}{\partial x_i}\right\rangle \quad \text{and} \quad \varepsilon_k = \frac{1}{2}\varepsilon_{ii}. \tag{8}$$

Considering the estimation of Pope [77], the maximum dissipation takes place at a length scale of about $24l_c$. Since at least two grid points are needed to resolve a flow feature, a grid spacing of $h_{max} \leqslant 12l_c$ is required. Due to the low Prandtl number in the present case, the turbulent structures of the velocity field are much smaller than those of the thermal field. Hence, the resolution requirement is determined by the velocity field and not by the temperature field. Thus, the Reynolds number was chosen for the scaling. Owing to the fact that the flow is dominated by buoyancy, and the characteristic velocity is defined accordingly (see Section 2), one could also take the Grashof number for the scaling.

The dissipation rate ε_k is not known a priori, as it is computed from flow quantities. Thus, it was estimated from simulations in the literature, e.g. by Wagner [64]. Accordingly, the computational grid was firstly chosen to contain 8,388,608 CVs, which is divided into 8 blocks with $128 \times 128 \times 64$ CVs each. Then from test simulations the actual dissipation rate ε_k was determined from the DNS to check if the resolution is sufficient. In the bulk of the melt, the dissipation rate is not very high, the overall average dimensionless value is $\langle\overline{\varepsilon_k}\rangle = 0.00544$, leading to a mean grid width of $h_{max} = 0.0138$ for the interior. Near the walls, however, the dissipation rate adopts much larger values up to a maximum of $\varepsilon_{k,max} = 0.466$ close to the crystal corner, which means an edge length of the CV of $h_{max} = 0.00458$. On the basis of the large discrepancy between the average and maximum value, the grid was refined towards the walls and the crystal region. A stretching ratio of 1.1 at most was applied to avoid convergence problems and to keep numerical errors small (see Section 3.2), such that the discretization scheme is still very close to second order accuracy despite the non-uniformity of the grid [72]. The actual mean grid width h, defined by $h = \sqrt[3]{\Delta x\Delta y\Delta z}$ under the assumption that the cells are nearly cubic, was directly compared to h_{max}. Values of $h/h_{max} \leqslant 1$ mean that according to the estimates of Kolmogorov and Pope, respectively, all turbulent scales of the flow are resolved. This is the case in the whole domain. Especially in the center of the crucible, the grid shows a very fine resolution with $h/h_{max} \leqslant 0.2$. Near the walls and the free surface as well as below the crystal, the dissipation is very high, so that the values of h/h_{max} are bigger, yet always below 0.7 and thus the computational cells are sufficiently small there.

Analogous to the characteristic length scale l_c for the estimation of the spatial resolution requirement, also a typical time scale t_c can be determined, using the following definition by Kolmogorov [75,76] in non-dimensional form:

$$t_c = \left(\frac{1}{\varepsilon_k Re}\right)^{\frac{1}{2}}. \quad (9)$$

With the computed value of $\varepsilon_{k,max}$, this gives a smallest time step of 6.76×10^{-3}. Due to the explicit time marching algorithm used here, the time step size had to be chosen as 2.5×10^{-4} for numerical stability, so that the Kolmogorov limit has already been achieved.

However, in the bulk of the melt the flow is far from being homogeneous and isotropic and thus the relation given can only provide a crude estimate. Furthermore, the largest values of h/h_{max} are found in the vicinity of the crucible walls. Especially in this near-wall region where the flow is strongly inhomogeneous and anisotropic, the second criterion mentioned above has to be taken into account. Owing to the low Prandtl number of the Si melt, the velocity boundary layer is expected to be much thinner than the thermal boundary layer and thus has to be checked in detail.

To verify the sufficiency of the resolution in the critical near-wall regions, the minimum non-dimensional wall-distances n^+ were calculated using the time-averaged wall shear stress $\langle \tau_w \rangle$:

$$n^+ = x_n \langle u_\tau \rangle Re = x_n \sqrt{\frac{\langle \tau_w \rangle}{\rho}} Re = x_n \sqrt{\frac{1}{Re} \frac{\partial \langle u_{par} \rangle}{\partial x_n}} Re, \quad (10)$$

where n denotes the dimensionless normal distance from the wall (this corresponds to the coordinates y or z, respectively), $\langle u_\tau \rangle$ the averaged wall shear stress velocity, and $\langle u_{par} \rangle$ the averaged total magnitude of wall-parallel velocities. In Fig. 2 it can be seen that the values of y^+ and z^+ are ranging up to 1.4 at the bottom and at the sidewall with most values below unity, which are reasonable values, proving that the resolution at the walls is sufficient. Below the crystal, the values are larger due to the high shear induced by the counterrotation, with a maximum z^+ of about 7. This can be denoted as too high, however, this region is very small compared to the rest of the domain, and an increase of the grid resolution would add enormously to the computational power needed without an adequate benefit. So the overall mesh size can be stated as sufficient, and in comparison with previous simulations available in the literature, the resolution is strongly improved.

This fact is also confirmed when the thickness of the boundary layers is estimated. In Fig. 3, the dimensionless averaged velocity profiles $u^+ = \langle u_{par} \rangle / \langle u_\tau \rangle$ at several positions at the crucible bottom, the sidewall and below the crystal are shown. In the graphs, the positions of the cell centers of the numerical grid are indicated as vertical or horizontal lines. It can be deduced that, except maybe below the crystal, at least 3 CVs are in the viscous sublayer, which extends from the wall to approximately $n^+ = 5$ and can be identified through the linear velocity profile. As mentioned above, by virtue of the low Prandtl number, the temperature boundary layer is much thicker and thus is automatically resolved well.

The thickness of the viscous sublayer was chosen as an a priori estimation of the resolution required and researched for in the literature. Unfortunately, boundary layers in low-*Pr* convection are rarely investigated. To the authors' knowledge, Cioni et al. [17] are the only ones to mention a specific formula for the thickness of the viscous sublayer λ_v in R–B convection in mercury: $\lambda_v/L \approx 140/Re$ with a characteristic length scale L. With the values of the present case, a value of $\lambda_v/L = 0.003$ can be deduced, which corresponds to $\lambda_v = 0.51$ mm. This agrees quite well with the results of the present simulations, where the end of the viscous sublayer, i.e. the linear relation, at $y^+ = 5$ approximately collapses with the coordinate value of $z/R_c = 0.005$ at the bottom of the crucible. Takeshita et al. [22] also conducted experiments with R–B convection in mercury, but the boundary layer thickness they measured (2.7 mm in a cell of 10 cm height) is defined in a different way, suggesting that it might be for the full boundary layer, not just for the viscous sublayer. The same applies to the results of simulations by Verzicco and Camussi [19], who obtained a value of about 4.6 mm for the boundary layer thickness. As these values are the only usable data from the literature, it can be concluded

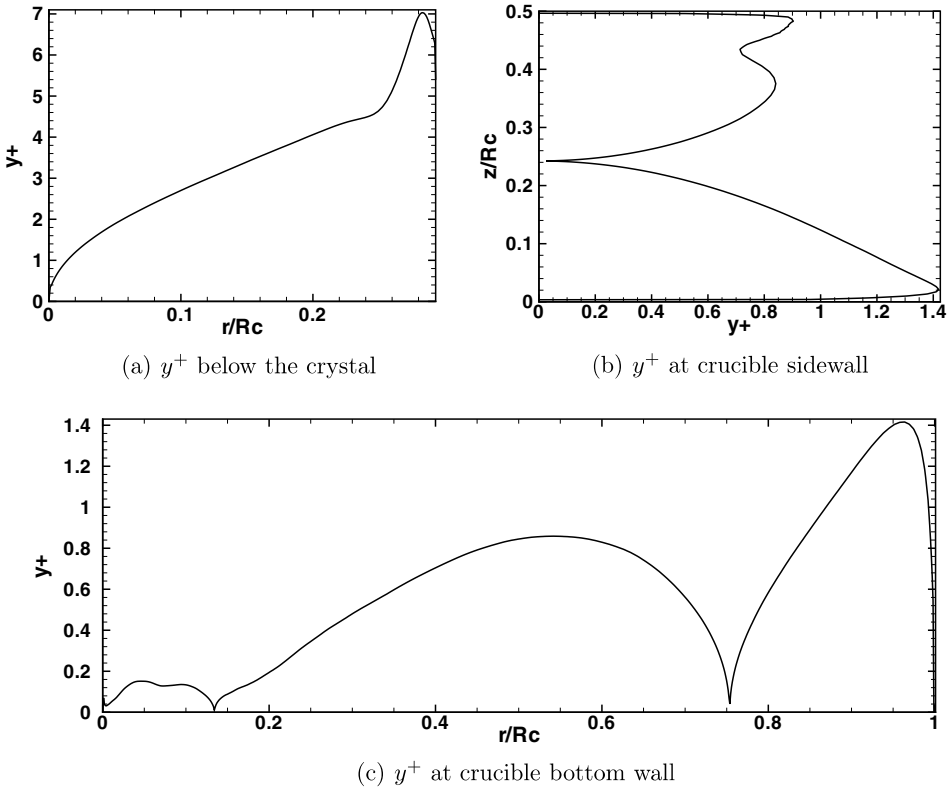

(a) y^+ below the crystal

(b) y^+ at crucible sidewall

(c) y^+ at crucible bottom wall

Fig. 2. Values of y^+ (a) below the crystal, (b) at the crucible sidewall, and (c) at the crucible bottom wall. Calculated from circumferentially and time-averaged quantities.

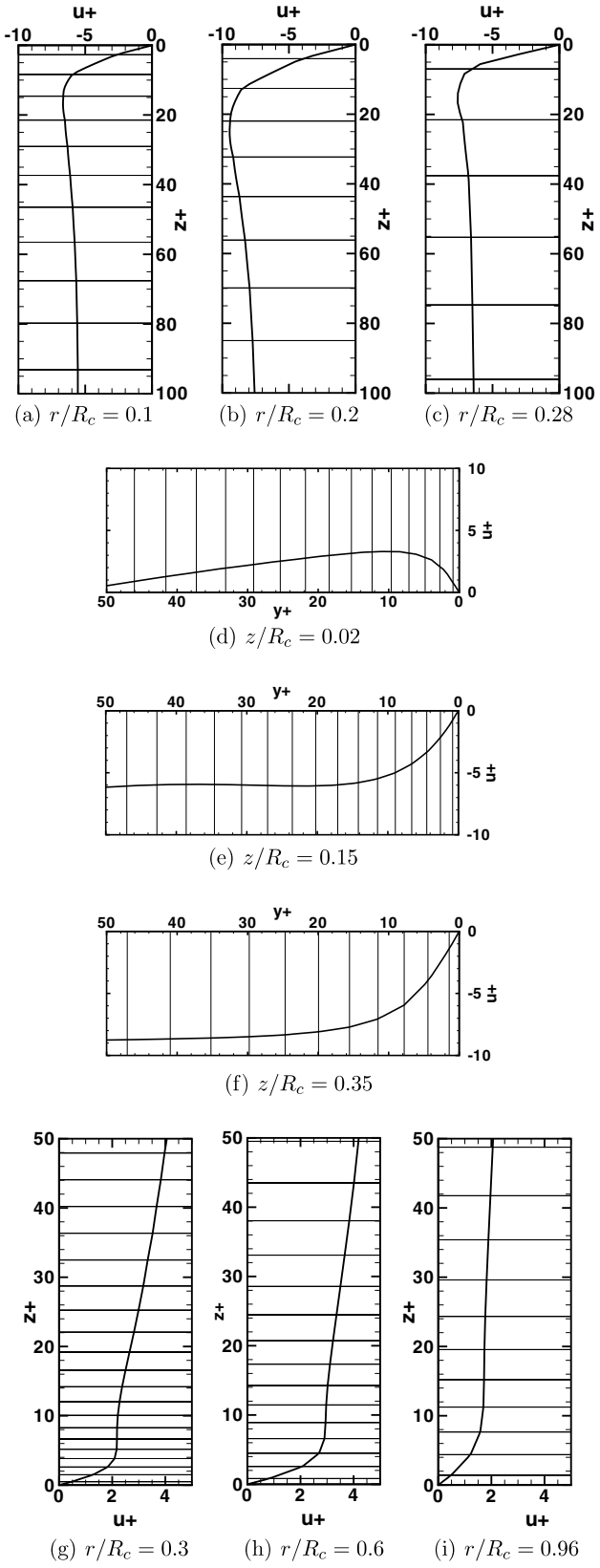

Fig. 3. Dimensionless velocity profiles (a)–(c) below the crystal, (d)–(f) at the crucible sidewall, and (g)–(i) at the crucible bottom wall. Calculated from circumferentially and time-averaged quantities.

that boundary layers especially in low-*Pr* fluids must still be subject of investigation. Due to the lack of data, for the estimation of the resolution requirements of the near-wall regions, different approximations can be found in the literature. Grötzbach [78] analyzed this topic in depth, and his derived criteria were used by several authors (e.g. Verzicco and Camussi [19]). However, they are based on several assumptions only valid for high- or moderate-*Pr* fluids, e.g. that the thermal turbulent structures and boundary layer thickness is the reference scale, which is not true for the present Cz configuration at low-*Pr*. Thus the resolution requirements in the present study have to rely on the criteria described above showing that a sufficient resolution of the boundary layers could be achieved, as can be concluded from the profiles in Fig. 3.

4.2. Grid topology and structure

The division of a cylindrical geometry into hexahedral CVs for the structured computational grid can be achieved by several ways. This topic was addressed in detail by Basu et al. [46]. In order to avoid the singularities of a one-block polar grid or the one-block barrel grid, which is a Cartesian grid fit to the circular shape, an O-grid type mesh was chosen, i.e. one almost cubic block is placed in the center of the cylinder, which is connected to the outer part by a polar grid (see Fig. 1). As shown in [46], this grid topology leads to a high-quality grid preventing convergence problems and assuming low numerical errors. To take advantage of the architecture of the supercomputer on which the calculations were carried out, consisting of 8 processors per node, the grid was designed to have 8 blocks. Consequently, the inner block of the O-grid was split in half, so that it became a dodecaedral structure with six outer blocks. To avoid highly skewed cells which are detrimental for the convergence and accuracy of the solution, the grid was smoothed using a Hilgenstock–Laplace and a Sörensen–Laplace algorithm, which are preserving the cell heights at the boundaries and improving the orthogonality while trying to find an equal node distribution in the inner region. The resulting grid shows a quality improvement especially in the vicinity of the corners of the O-grid, where the cells are less skewed and smooth transitions across the block boundaries could be achieved.

5. Case details

For the DNS, a dimensionless time step size of $\Delta t u_b/R_c = 2.5 \times 10^{-4}$, which corresponds to about 4.5×10^{-4} s of real time, was chosen, resulting in a maximum CFL number of about 0.18 throughout the computation. Due to the complexity of the flow it is hard to identify characteristic structures from the instantaneous velocity and temperature fields. Therefore, the results were averaged in time and additionally in circumferential direction. This provides also higher-order statistics such as Reynolds stresses relevant for turbulence analysis. To allow the flow and heat transfer to reach a fully developed turbulent state, the averaging procedure for the DNS was not started until a time of approximately 66 dimensionless units, which is identical to 10 crucible revolutions or 2 min of real time. The averaging process was then run for more than 4.3 million time steps, which equals 1080 dimensionless units of simulation time, 32 min of real time or more than 160 crucible revolutions, factoring in every 10th time step. Even higher-order statistics such as the dissipation tensor were computed, starting from a dimensionless time of more than 260 units (equal to more than 40 crucible revolutions), running for more than 800 units (120 revolutions). This exceedingly long averaging period was necessary due to the fact that large, slowly moving vortical structures were observed in the melt flow, which hampered a fast attainment of well-averaged data. This issue will be discussed more detailed in Section 6.1.

The DNS was run on the NEC SX-8 vector computer at the HLRS in Stuttgart, using one node with 8 processors according to the block-structure of the grid. A very high average computing efficiency of 8.2 GFlop/s per processor (more than 50% of the peak performance) could be achieved. The whole simulation took more than 1000 hours of real time.

6. Results and discussion

6.1. Dynamic behavior

Due to the turbulent nature, and thus the instationary and three-dimensional behavior of the flow and heat transfer in the Si melt, it is hard to gain information from the vast amount of data. However, the analysis of the dynamics of the flow and heat transfer is very important, as the resulting effects act locally and punctual in time, not on an averaged basis, in a transient process such as the Cz crystal growth. Thus, not the overall flow structure will be described looking at the instantaneous data, but only important phenomena will be discussed.

Due to the boundary conditions of the case and the resulting high dimensionless numbers, *Re*, *Ra*, and *Ma*, the flow and heat transfer is fully turbulent and thus beyond the limits of laminar flow structures and regular or periodic patterns, caused by certain instabilities such as Bénard cells, waves etc., as described by Ristorcelli and Lumley [42] and others. In fact, the structure of the flow and heat transfer in the melt is dominated by the irregular forming of buoyant plumes, carrying hot fluid from the bottom or side of the heated crucible towards the cold crystal or the free surface, which is cooled by thermal radiation. This can clearly be seen in Fig. 4a, depicting a snapshot of the temperature distribution at the free surface. These plumes or hot spots were also reported in the literature by other researchers conducting simulations or experiments, see e.g. [48,46]. Kishida et al. [61] attributed these "polka dots" to geostrophic turbulence caused by strong Coriolis forces occurring at high rotation rates which counteract the buoyant flow and thus destroy regular patterns like baroclinic waves. In their experiments, characteristic features of such geostrophic turbulence were observed. Contrarily, Enger [51] located the flow pattern in a non-geostrophic turbulence regime, according to the instability map of Fein and Pfeffer [79], who were investigating flows in a rotating annulus. However, the Rossby number of the melt flow is quite low ($Ro = 0.62$ [51]), such that in this map the flow would actually be located in the region of geostrophic turbulence. But the state of geostrophic turbulence is reported to be characterized by irregular waves, which contradicts the flow pattern observations by Enger [51] and also in the present case. Furthermore, Kakimoto et al. [80] mentioned differences of their

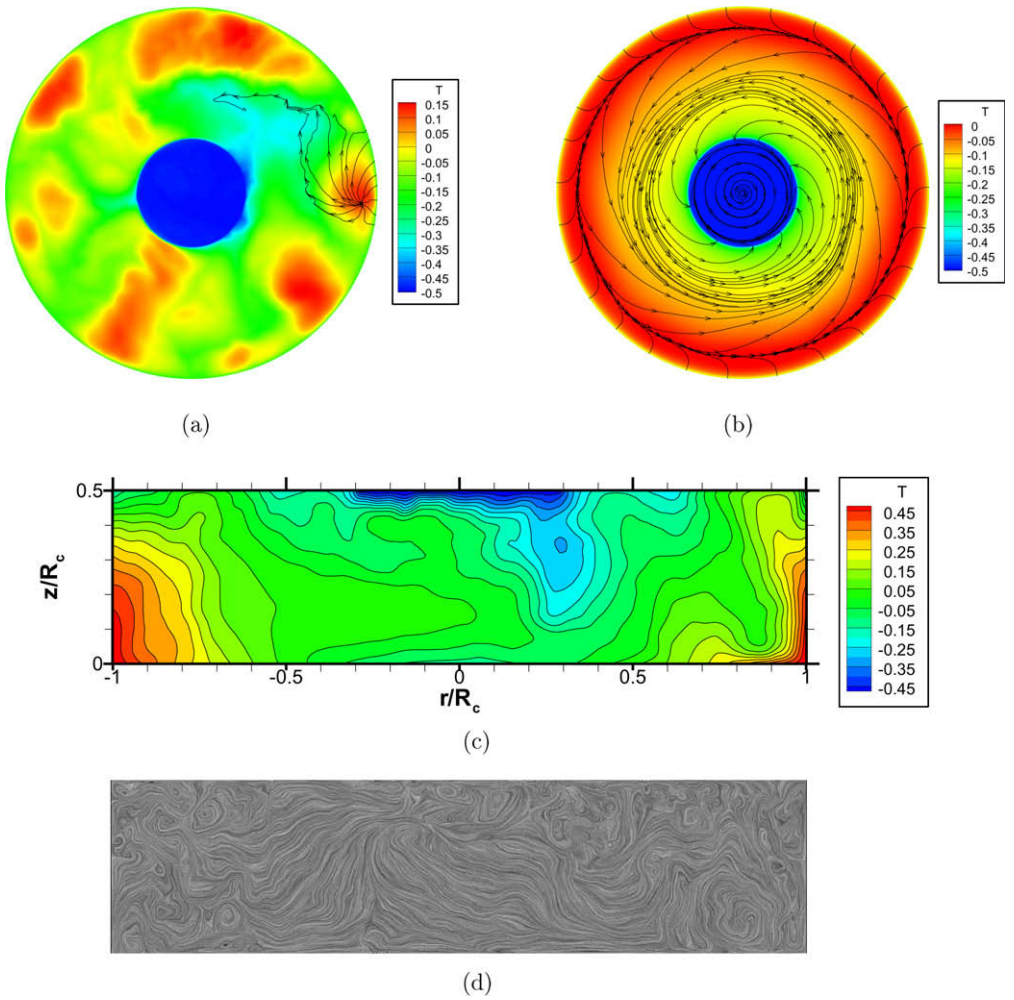

Fig. 4. Instantaneous (a) and mean (b) temperature distribution with streamlines at the free surface. In the center, the cold counterrotating crystal is located. At the free surface, thermal plumes can be identified. The mean distribution shows that the melt flow is directed inwards. In the outer region, where the streamlines diverge, thermal plumes appear preferably. Furthermore, the instantaneous temperature distribution (c) and LIC velocity field (d) in a vertical cut through the crucible ($y = 0$) depict the small velocity structures in contrast to the larger temperature scales.

observations regarding geostrophic turbulence from an instability map by Fowlis and Hide [81], which is similar to the one by Fein and Pfeffer [79]. Thus it can be concluded that the results from experiments with rotating annuli cannot be compared with the Cz–Si simulations, presumably due to the different geometry.

At the free surface, the hot fluid is carried from the center of the plumes outwards to the cooler regions, which is depicted in Fig. 4a by the streamlines. This is the Marangoni effect, caused by the difference in surface tension between hot and cold fluid. The plumes are not restricted to certain dimensions, but can also extend over larger regions. However, they preferably do not appear in the vicinity of the crystal, but closer to the crucible wall, as can be seen from the mean streamlines in Fig. 4b.

Around the center of the crucible, a large vortical structure forms (see Fig. 5). This is caused by the interaction of the crucible rotation inducing centrifugal and Coriolis forces and the buoyancy, leading to a spiral or swirling flow directed towards the center and the bottom, which is typical for the rotating disc problem. It was also observed by Jones et al. [82]. This structure remains stable throughout the whole process, moving very slowly with respect to the crucible in the same direction of rotation. In Fig. 5, the movement is depicted by six consecutive snapshots of the pressure contours in a horizontal cut through the middle of the crucible. The time period between the first and sixth snapshot represents a half rotation of the structure corresponding to about 7.5 crucible revolutions. From the pressure contours and the streamlines in this plane, it can also be seen that the vortex itself rotates in counterclockwise direction like the melt, with the center of rotation slightly off the axis of the crucible, or even split up into two vortices. The fact that this large structure is moving faster than the crucible rotation can be explained by momentum conservation. The buoyancy and surface tension forces create an overall melt flow towards the center of the crucible (see Fig. 4b), which causes an accelerated rotation of the fluid. This phenomenon of stable eddies was also observed in experiments with Cz–Si using X-ray radiography by Kakimoto et al. [44], who attributed it to baroclinic instability and geostrophic turbulence in the melt flow.

In Fig. 4c and d, an instantaneous temperature distribution and velocity field (using the Line-Integral Convolution method (LIC)) are shown in a vertical cut through the crucible. It can clearly be seen that according to the small Prandtl number of the Si melt, the turbulent scales of the temperature field are much larger than the scales of the velocity field. The flow field breaks up into very small vortices where the kinetic energy is finally dissipated into heat.

6.2. Time-averaged quantities

For the analysis of the statistical behavior of the melt, the velocity and temperature fields were averaged in time. For a cylindrical geometry, one would expect an axisymmetric result, if the averaging time is sufficiently long. In the present case, the amount of more than four million time steps representing more than half an hour of real time seems to be very high as it is far more than the simulations from the literature known to the authors. However, as could be seen in the previous section, large vortical structures evolve in the melt flow, moving very slowly around in the crucible, being almost stationary, and thus disturbing the averaging procedure massively. Therefore, in the mean fields of temperature and velocities, still small asymmetries can be identified even after the long simulation and averaging period. To level these asymmetries out, the averaging process would have to be carried out over an enormous time period, which cannot be achieved in an acceptable time even with today's high-performance computing facilities. To overcome this problem, axisymmetry of all statistical data was established through additional averaging in circumferential direction, so that the different quantities are presented in a vertical half-slice of the crucible (see Figs. 6–8), where the sidewall is located on the right and the central axis on the left. The crystal extends from the center to the dimensionless radius $r/R_c = 0.294$ at the top, the remaining part is the free surface.

Figs. 6–8 present an overview of the results of the DNS prediction for the temperature and flow field, respectively. The averaged temperature contours show that the heater provides the maximum heat flux at the lower edge of the crucible, decreasing towards the center and the top (Fig. 6a). The heat is transported through the bulk of the melt, and finally lost at the free surface through thermal radiation, or at the cooler solid crystal. The radiation effect is indicated by the trend of the isotherms exhibiting a certain angle to the free surface. It is relatively small compared to the cooling of the crystal due to the high ambient temperature as can be seen from the bunching of isotherms below the crystal. Although at this high Rayleigh number the convective heat transport is much larger than the conductive, the averaged temperature distribution shows a pattern similar to conduction-dominated heat transfer with a smooth gradient from the hot wall to the cool crystal. This originates from the fact that the thermal turbulent scales are quite large at the low Prandtl number considered so that smaller structures are ruled out.

From the streamlines in Fig. 6e, the characteristic structure of the statistically averaged flow field can be observed, which consists of three large convection rolls (denoted **A**, **B**, and **C**) extending over the whole height of the melt and one secondary vortex at the top of the sidewall (denoted **D**). This is typical for a system similar to rotating Bénard–Marangoni, where buoyancy, centrifugal and Coriolis forces as well as Marangoni convection interact. In a pure Bénard system, a layer of colder fluid is located above one of warmer fluid, which causes instability due to buoyancy and thus the formation of so-called Bénard cells, which circulate from the top to the bottom of the melt. This phenomenon can be seen at the lower part of the crucible sidewall, where through the high temperature from the heater, buoyant upward flow is dominating (roll **C**). However, owing to additional rotation and surface tension, the flow situation in the present configuration is much more complex than for pure buoyancy-driven flow. Close to the free surface, the sidewall is already colder than the melt, and the Marangoni effect becomes influential, which drives the flow towards the colder regions due to the change in surface tension. As a result, a counter-rotating vortex **D** forms at the upper crucible wall. However, the lower roll **C** continues to the free surface, winding around the smaller vortex **D**, because the temperature reaches a local maximum at about $r/R_c = 0.88$, and then decreases towards the center. Thus, the surface tension gradient and consequently the velocity at the surface change their sign. This point of the local temperature maximum is the region where thermal plumes appear on the free surface, driven by the buoyancy forces and supported by the Marangoni convection. In the top view of the melt surface, this can be identified in the mean velocity field at the location where the velocity changes its sign (see Fig. 4b). In the instantaneous field, hot-spots or islands can be seen there (see Fig. 4a), as mentioned in the previous section. The strong flow induced by the surface tension continues to the corner of the crystal and slightly further underneath it, but the shear layer below the free surface is very thin, so that the influence on the bulk flow remains small. Right below the crystal, owing to the rotation an Ekman layer is formed, which is a viscous boundary layer for rotation. It is very thin, see the enlargement of the area in Fig. 6f. The flow inside the boundary layer is obviously dominated by centrifugal forces, as the velocity vectors are directed outwards despite the counteracting velocity of the large vortex **A** below the crystal. In Fig. 6f, it can be seen that due to the change in flow direction another small vortex is generated near the edge of the crystal, which does not

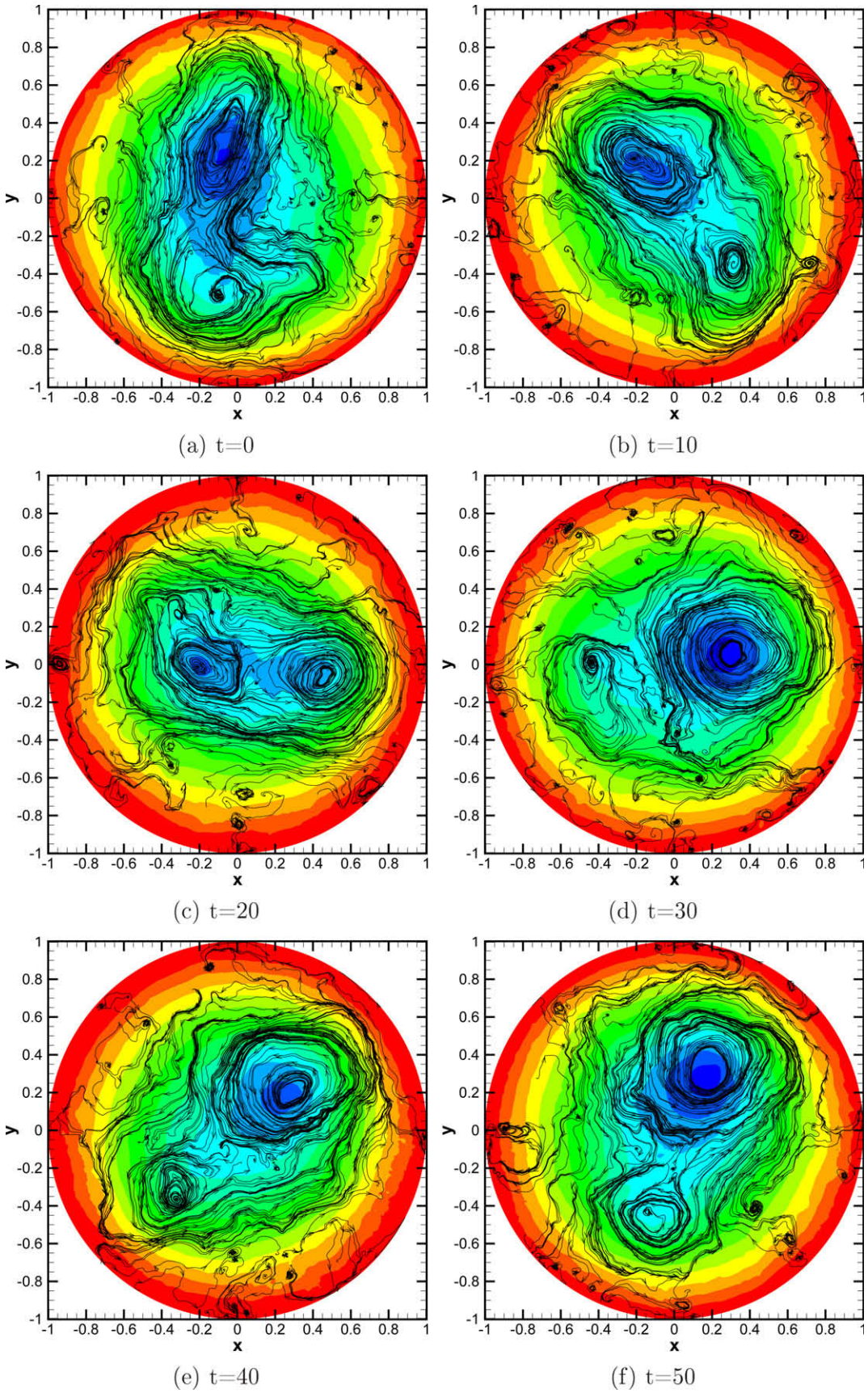

Fig. 5. Instantaneous pressure contours and streamlines in the melt in a horizontal cut through the crucible ($z/R_c = 0.25$). The crucible is rotating in counter-clockwise direction, the pictures show the movement relative to it. Intervals of 10 dimensionless time units ($\approx$ 18 s or 1.5 crucible revolutions) are between consecutive pictures (from top left to bottom right line by line), giving a total time of 50 dimensionless units or $\approx$ 90 s or 7.5 rev., while the large vortical structure moves less than one half revolution relative to the crucible.

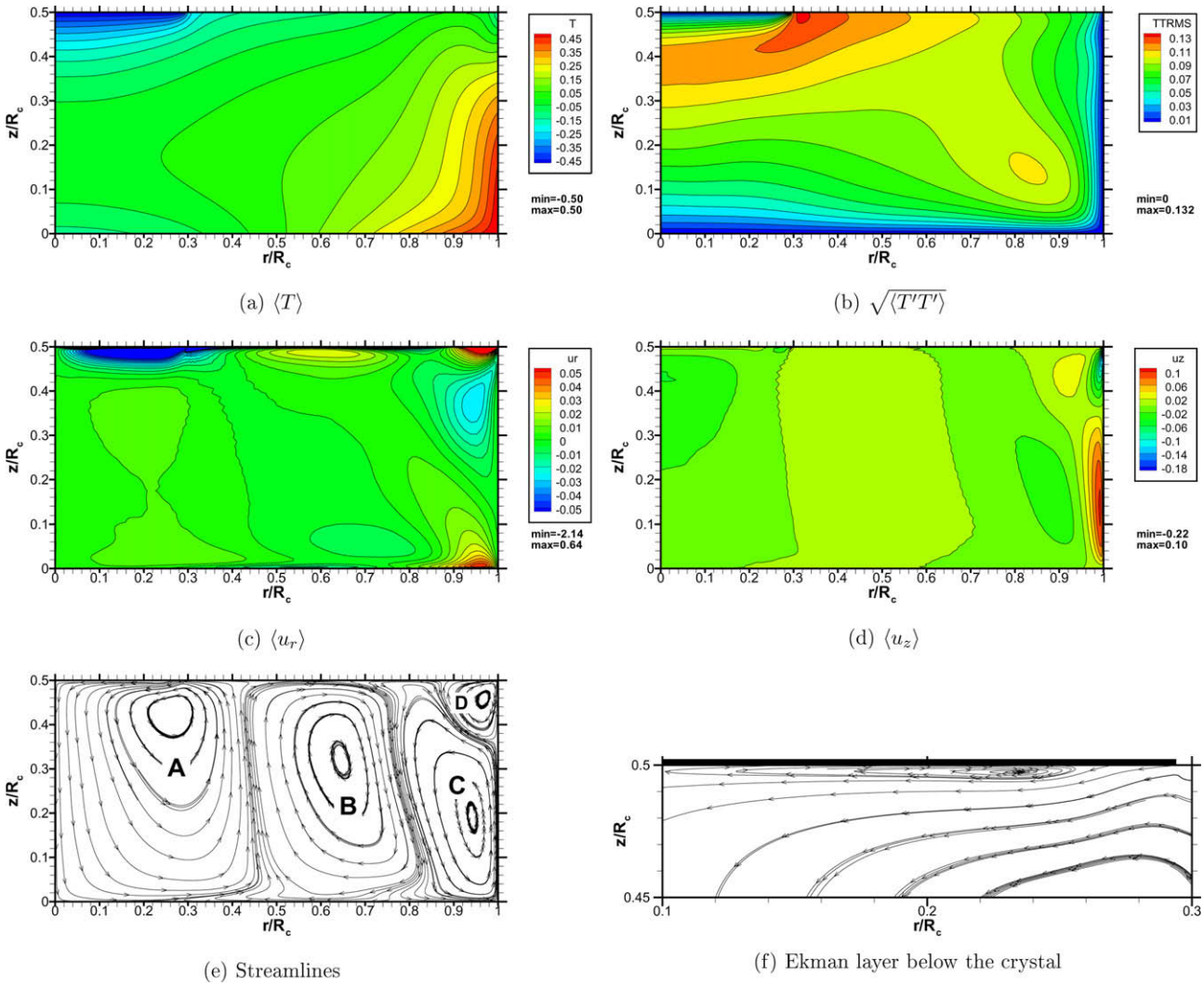

Fig. 6. Circumferentially and time-averaged temperature $\langle T \rangle$ and temperature fluctuations $\sqrt{\langle T'T' \rangle}$, velocities $\langle u_r \rangle$ and $\langle u_z \rangle$ and streamlines in the melt in a vertical cut through the center of the crucible (axis of symmetry on the left border, crucible wall on the right border).

have an impact on the bulk flow owing to its size. This phenomenon was not mentioned by Wagner [64], although by looking closely at his simulation results, one might be able to see such an Ekman layer with the small recirculation zone.

The crystal can be seen as a rotating disc, so apart from the Ekman layer, a big vortex **A** is forming below called a Taylor–Proudman cell, which is induced by centrifugal forces competing with the radial pressure gradient. As mentioned in the previous section, the rotating disc induces spiral flow, which cannot be depicted in this two-dimensional vertical cut, neglecting the flow in circumferential direction, and which is also ruled out through the averaging procedure. At the central axis the downward flow is also induced by the negative buoyancy through the temperature difference between the cold crystal and the heated bottom. At the bottom, another Ekman layer is formed through the rotation.

The vortex **B** in the middle of the depicted crucible-half (see Fig. 6e) is a product of the Taylor–Proudman cell **A** and the buoyant Bénard cell **C** at the sidewall. The Taylor–Proudman cell from the rotating crystal, supported by the negative buoyancy, moves the cold melt to the bottom, which has to move upwards again at some point to conserve the mass and momentum. The buoyant cell at the sidewall does move the fluid upwards, however, at this aspect ratio (H/R = 0.5) of the crucible, a Bénard cell embracing the whole radius is not stable. Thus, the vortex is split up, and another roll **B** in between both vortices **A** and **C** is formed to account for the opposing flow directions. From the contour plots of the velocities (Fig. 6), one can see that the values in the bulk of the melt are very low, so the structure in the middle is indifferent, which can also be concluded by looking at the fluctuations as will be done in the next section. Only the radial movement below the crystal towards the center and in opposite direction at the free surface near the wall as well as the axial upward flow at the sidewall are of significant velocity magnitude. The observation of this vortex **B** is coincident with the finding of an additional vortex induced by the thermocapillary forces as mentioned in Kumar et al. [83].

The above described overall flow structure containing four major vortices resembles closely the simulation results of Wagner [64], who computed a very similar case, as already mentioned. Nevertheless, some differences are present: Wagner counts five vortices in his plot showing streamlines of the averaged flow field. However, a combination of two of them could be comparable to vortex **C**, only stretching further out along the free surface. Furthermore, the analogon to vortex **B** extends further along the bottom. This can be caused by Wagner's slightly different conditions such as a coefficient of thermal expansion of $\beta = 1.0 \times 10^{-4}\,\mathrm{K}^{-1}$ and the approximation of the thermal radiation from the free surface by a fixed heat flux.

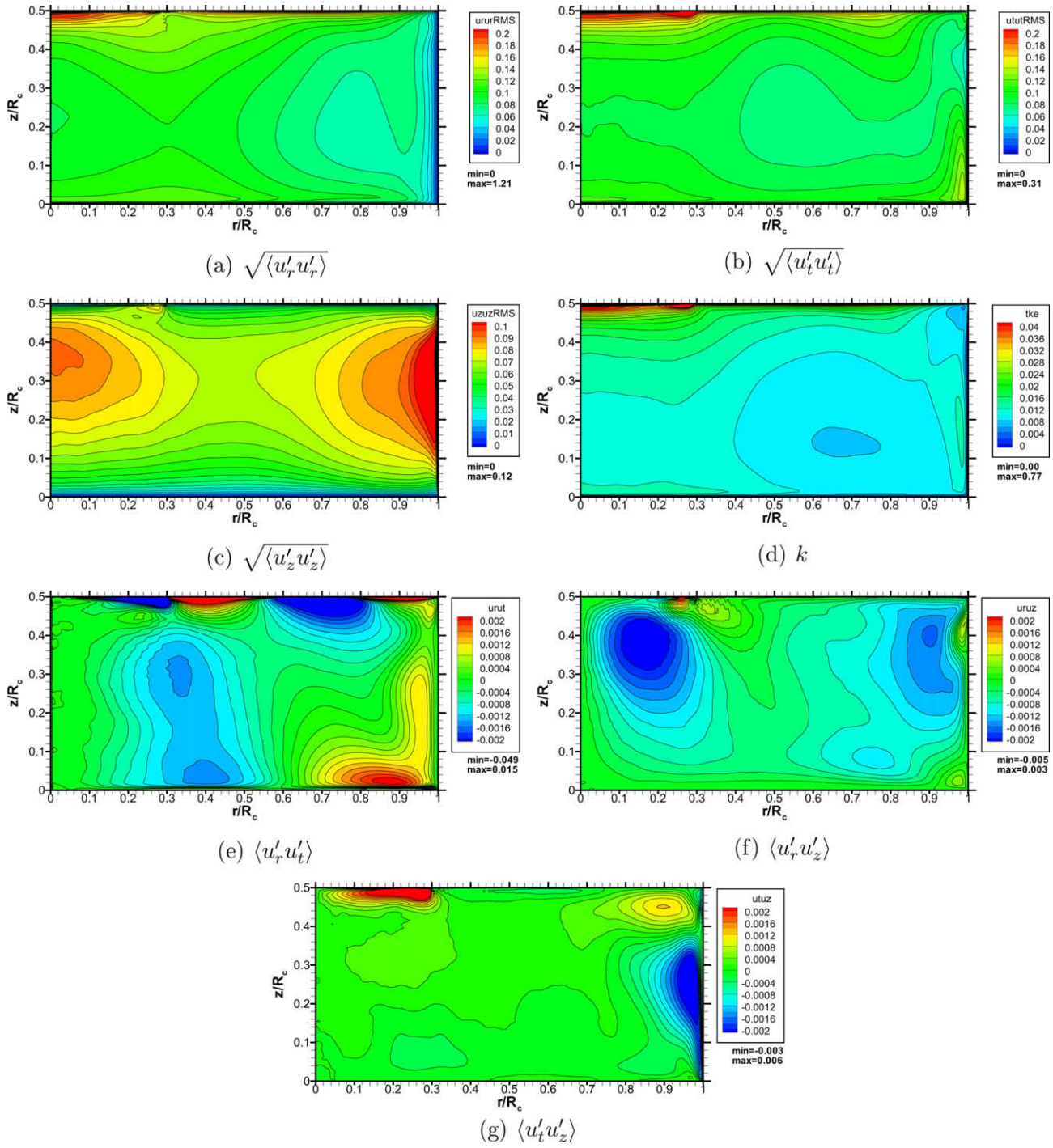

Fig. 7. Circumferentially and time-averaged RMS velocity fluctuations $\sqrt{\langle u_r' u_r' \rangle}$, $\sqrt{\langle u_t' u_t' \rangle}$, $\sqrt{\langle u_z' u_z' \rangle}$, turbulent kinetic energy k and mixed velocity fluctuations $\langle u_r' u_t' \rangle$, $\langle u_r' u_z' \rangle$, and $\langle u_t' u_z' \rangle$ in the melt in a vertical cut through the center of the crucible (axis of symmetry on the left border, crucible wall on the right border).

The Cz–Si case using a realistic crucible geometry simulated by Kumar et al. [83] served as a basis for Wagner's and the present idealized case. In a direct comparison, one can see a similar flow structure exhibiting the main features mentioned in this section, containing large convection rolls. The buoyant vortex **C** at the wall could be identified as well as the smaller recirculation zone **D**. However, due to the different geometry, the shape of the vortices do not completely coincide with the present results. Also, the fact that the data in [83] are not averaged in circumferential direction, complicates the comparison. Moreover, the case was simulated using a very coarse grid in relation to the present DNS, such that some flow features, especially those invoked by turbulence, may not have been resolved.

6.3. Temperature fluctuations and Reynolds stresses

From the statistical data, besides the averaged values, also fluctuations are obtained. These are characteristic for turbulence. The correlations between the different velocity fluctuations form the Reynolds stress tensor. In Fig. 6b it can be seen that the averaged root mean square (RMS) temperature fluctuations $\sqrt{\langle T'T' \rangle}$ tend to zero at the crucible walls due to the fact that a fixed temperature

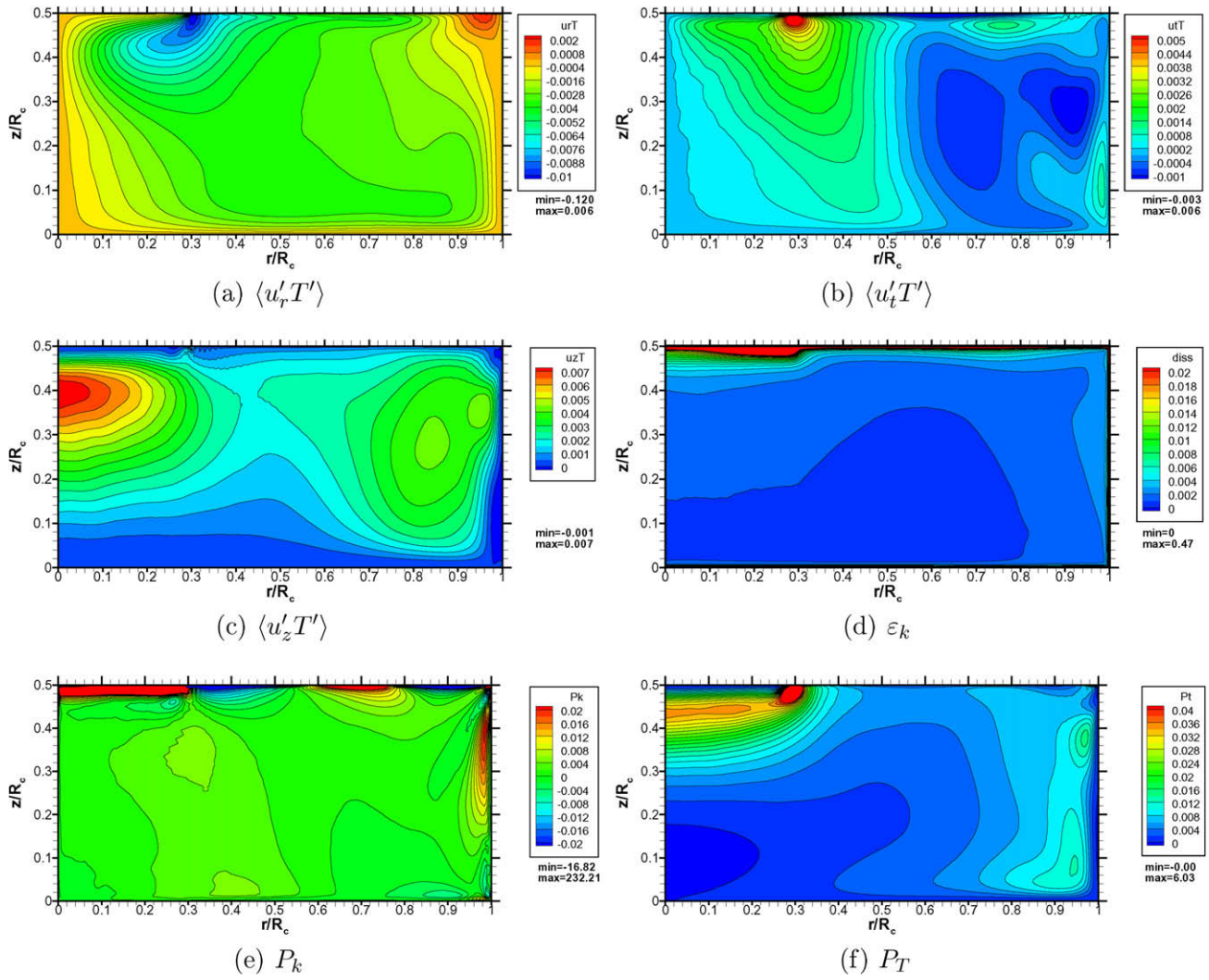

Fig. 8. Circumferentially and time-averaged turbulent heat fluxes $\langle u_r' T' \rangle$, $\langle u_t' T' \rangle$, and $\langle u_z' T' \rangle$, and viscous dissipation rate ε_k and production terms P_k and P_T in the melt in a vertical cut through the center of the crucible (axis of symmetry on the left border, crucible wall on the right border).

profile is applied there. Also at the crystal, the temperature is fixed to the melting temperature, and thus the fluctuations show very small values in its vicinity. However, at the corner of the crystal, where the free surface of the melt starts, the maximum fluctuation is located. This is caused by the large temperature difference between the free surface and the crystal, which induces a strong Marangoni flow at the surface, counteracting the centrifugal forces due to the rotation of the fluid (see Section 6.4). At this location, there is also an abrupt change in the heat flux density, with the cooling of the crystal on one side, and the thermal radiation from the free surface on the other side, which adds to the unsteadiness of the temperature. Furthermore, the high rotation rate of the crystal leads to high shear rates and thus an anisotropic flow in the vicinity of the crystal, which also increases the temperature fluctuations in this region. The location of the maximum temperature fluctuation at the corner of the crystal agrees with the results of Wagner [64] and Kumar et al. [83].

The RMS values of the velocity fluctuations representing the normal Reynolds stresses are depicted in Fig. 7. From the range of the values compared with those of the averaged velocities, it can be noticed that the fluctuations are in some regions much higher than the actual velocities. From this fact it becomes clear that the flow in the Si melt is highly instationary. The variations of the radial and tangential velocities show their maxima at the free surface, where the strong Marangoni convection takes place and competes with the buoyant and centrifugal forces, and below the crystal, where strong shear is induced by the rotation of the crystal. Near the walls, the values of $\sqrt{\langle u_i' u_i' \rangle}$ naturally tend to zero. Nevertheless, the tangential component $\sqrt{\langle u_t' u_t' \rangle}$ shows strong fluctuations around the lower corner of the crucible, although one would suggest quite a steady flow due to the rotation of the crucible. Yet, in this area the highest temperatures are present, so that the induced buoyancy is very strong and causes high fluctuations, which on the other hand are relatively small compared to the absolute velocities (see Fig. 6). The same applies to the vertical component $\sqrt{\langle u_z' u_z' \rangle}$ near the sidewall, where the maximum fluctuation is located corresponding to the high average value of $\langle u_z \rangle$. In the vicinity of the central axis of the crucible, also high fluctuations are present due to the strong temperature changes, as mentioned above, causing unsteady buoyant flow in combination with the effects of rotation. The overall absolute values of $\sqrt{\langle u_z' u_z' \rangle}$ are significantly smaller than the other fluctuations, which is partially caused by the shallow geometry, limiting the buoyant forces compared to the Marangoni and Coriolis forces due to the rotation.

The turbulent kinetic energy, depicted in Fig. 7d, is defined as the trace of the Reynolds stress tensor: $k = 1/2 \langle u_i' u_i' \rangle$ and is a good measure of the overall contents of turbulence in the melt due to flow. As expected from the plots of the single fluctuations, the

maximum turbulent kinetic energy is located at the free surface and below the crystal, where the highest shear rates occur and the flow is highly instationary. At the walls, the values of k are very low due to the boundary layers.

The values of the mixed correlations of the velocity fluctuations representing the Reynolds shear stresses (Fig. 7e–g) are about one order of magnitude smaller than the main Reynolds stresses (the squared values $\langle u_i' u_i' \rangle$, not the RMS values), so their accuracy may be lower than for the normal stresses. Clearly, in the combination of radial and tangential fluctuations, the strong Marangoni effect at the free surface can be recognized. In the plot of $\langle u_r' u_z' \rangle$ and $\langle u_t' u_z' \rangle$, it can be seen that the fluctuations at the corner of and below the rotating crystal as well as at the sidewall, where the strong buoyant vortex **C** and the recirculation zone **D** are located, are dominant.

The mixed velocity–temperature correlations $\langle u_i' T' \rangle$ represent turbulent heat fluxes and can be used to characterize the heat transport in the melt due to turbulence (see Fig. 8a–c). In radial direction, the heat transport $\langle u_r' T' \rangle$ shows the largest absolute values at the corner of the crystal, corresponding to the strong velocity and temperature gradients due to the counterrotation of the crystal and the transition of the melt from the hot free surface towards the cooler crystal. Another peak is located at the free surface near the crucible sidewall, where through the rising buoyant plumes temperature and velocity differences occur. However, the absolute magnitude of the heat flux there is about one order smaller than at the corner of the crystal. At the sidewalls and bottom, the values are near zero due to the fixed crucible temperature.

In tangential direction, the maximum heat flux $\langle u_t' T' \rangle$ can also be found near the edge of the crystal for the same reason as mentioned above for the radial flux. Another region with high absolute values is located close to the sidewall where the tangential velocity is large due to the crucible rotation and thus the fluctuations are relatively high.

The vertical turbulent heat flux $\langle u_z' T' \rangle$ shows its highest values below the center of the crystal, which originates from the strong temperature differences and the resulting instationary buoyant flow there. This corresponds well with the plots of the temperature and vertical velocity variances (Figs. 6b and 7c). Relatively high values can also be detected at the location of the strong buoyant vortex **C** near the sidewall of the crucible. The heat flux tends to zero near the bottom and the free surface due to the fact that there is no vertical velocity, and also the temperature distribution is stable.

6.4. Budgets

It is a characteristic property of turbulence that the kinetic energy of the flow is finally dissipated into heat. Thus the dissipation rate of the turbulent kinetic energy ε_k, as defined in Eq. (8), is a good measure for the amount of turbulence contained in a flow. In the present case, the dissipation almost exclusively takes place below the crystal and at the free surface (see Fig. 8d), as one could have suggested from the preceding analysis of the Reynolds stresses and the distribution of turbulent kinetic energy k itself.

Deriving the whole transport equation for k by contracting the indices of the equation for the Reynolds stresses, one obtains besides the dissipation rate also terms for diffusion, stress production and buoyancy production. The dissipation rate ε_k, the stress production P_k and the buoyancy production G_k are the most interesting terms in this balance. The remaining definitions are as follows:

$$P_k = -\langle u_i' u_j' \rangle \frac{\partial \langle u_i \rangle}{\partial x_j} \quad \text{and} \quad G_k = -\frac{Gr}{Re^2} \langle u_i' T' \rangle. \tag{11}$$

From the operating conditions of the present case, the fraction of the dimensionless numbers Gr/Re^2 can be calculated to approximately 1. Thus, considering the fact that the gravitational force only acts in z-direction, the buoyancy term G_k is identical to the vertical turbulent heat flux $\langle u_z' T' \rangle$, which is depicted in Fig. 8(c) and has already been discussed in the previous section.

The stress production term P_k is shown in Fig. 8e. According to its definition, the highest absolute values can be found where the steepest velocity gradients and the highest fluctuations occur. This is the case below the crystal and at the free surface corresponding to the strong changes in the radial and tangential velocity components, and at the sidewall, where the vertical velocity exhibits highly instationary behavior.

Similar to the Reynolds stress equation, an equation for the turbulent heat fluxes $\langle u_i' T' \rangle$ can be derived. Here, also different terms for diffusion, production, dissipation, etc. appear. For the present case, only the buoyancy production

$$G_T = \frac{Gr}{Re^2} \langle T' T' \rangle \tag{12}$$

should be considered. As mentioned before, the prefactor Gr/Re^2 is approximately 1, which leaves the buoyancy term G_T identical to the temperature fluctuation (see Fig. 6b) and thus is not shown here again.

Furthermore, an equation for the temperature variance can be obtained by multiplying the equation for the instantaneous temperature by T' and time-averaging it afterwards. The arising term for the production by the mean temperature gradient

$$P_T = -2 \langle u_i' T' \rangle \frac{\partial \langle T \rangle}{\partial x_i} \tag{13}$$

contains valuable information about the budget of turbulence and can be compared to the stress production term of Eq. (11). Due to the derivation from the temperature equation, no buoyancy term like G_T appears. In Fig. 8f the high accordance of P_T to the RMS temperature variance $\sqrt{\langle T' T' \rangle}$ (see Fig. 6b) with high values below the crystal can be seen. Furthermore, the position of the maximum value at the corner of the crystal matches the plots of the turbulent heat fluxes in radial and tangential direction.

Thus, the results are consistent with the definition of the turbulent quantities: The stress production P_k (production due to mean velocity gradient) corresponds to the velocity fluctuations, whereas the production due to the mean temperature gradient P_T is in accordance with the temperature variance.

7. Summary and conclusions

The results of a DNS of an idealized Cz–Si configuration were presented, which is a good example of rotating buoyancy- and surface-tension driven flow (Rayleigh-Bénard–Marangoni convection). This computation was carried out in order to gain a detailed insight in the structure of flows of this kind and also to obtain reference data for the validation of the LES method, which is used to reduce the computational effort of the predictions. Simulation results available in the literature were considered as either of insufficient accuracy or availability. The setup consists of a rotating cylindrical crucible of 170 mm radius, which contains the Si melt, with a disc-shaped crystal of 50 mm radius on top of the melt, which rotates in the opposite direction. Temperature boundary conditions were taken from experimental measurements, and the material properties of Si were applied. Thus, characteristic dimensionless numbers of $Re = 4.7 \times 10^4$, $Gr = 2.2 \times 10^9$, $Ma = 2.8 \times 10^4$, and $Ra = 2.8 \times 10^7$ were obtained, which are in the regime of fully turbulent flow.

In order to resolve all turbulent scales, a very fine computational grid of high quality was constructed with approximately 8.4×10^6 CVs. A grid study showed that the resolution was sufficient. The solution was obtained using a finite-volume scheme for curvilinear block-structured grids and an explicit time discretization. The code is highly parallelized and vectorized, and therefore runs very efficiently on supercomputers. As expected, the results exhibit a highly turbulent, instationary, three-dimensional flow and heat transfer in the melt, which is dominated by thermal plumes rising from the bottom of the crucible to the free surface. However, it was found that a large, stable vortical structure emerges around the center of the crucible and rotates slightly faster than the crucible itself. This hampered the averaging process, which was carried out to obtain statistical data for the turbulence analysis, and thus the simulations had to be run for a very long time. The collected time- and circumferentially averaged data show four characteristic Bénard cell-like vortices which evolve through the interaction of buoyant, Coriolis, and surface-tension forces. The temperature and velocity fluctuations have their maxima below the crystal, at the free surface, and especially around the corner of the crystal. Besides the Reynolds stresses and turbulent heat fluxes, also higher-order statistics such as the dissipation rate and the production terms due to the mean flow and buoyancy were analyzed. Besides, the DNS data will serve as a reference case for the validation of LES predictions within a subsequent paper.

Acknowledgements

The authors are grateful to the Bavarian State Ministry of Science, Research, and Art for their financial support in the KONWIHR framework (Competence Network for Technical-Scientific High- and Highest-Performance Computation). Furthermore, the authors would like to thank the HLRS (High Performance Computing Center Stuttgart) for the provision of computing time for the simulations under the grant number CZ/12761 and also their technical support. Finally, the authors appreciate the funding from the DFG (German Research Foundation) under the Grant Nos. DE 634/15-1 and BO 3107/1-1.

References

[1] H. Bénard, Les tourbillons cellulaires dans une nappe liquide. Première partie: description générale des phénomènes, Rev. Gén. Sci. Pure Appl. 12 (1900) 1261–1271.
[2] H. Bénard, Les tourbillons cellulaires dans une nappe liquide. Deuxième partie: procédé mécaniques et optiques d'examen. Lois numériques des phénomènes, Rev. Gén. Sci. Pure Appl. 12 (1900) 1309–1328.
[3] L. Rayleigh, On convection currents in a horizontal layer of fluid, when the higher temperature is on the under side, Philos. Mag. (1916) 519–546.
[4] E. Koschmieder, Bénard Cells and Taylor Vortices, first ed., Cambridge Monographs on Mechanics and Applied Mathematics, Cambridge University Press, Cambridge, 1993.
[5] A. Getling, Rayleigh–Bénard Convection, World Scientific, Singapore, 1998.
[6] O. Thual, Zero-Prandtl-number convection, J. Fluid Mech. 240 (1992) 229–258.
[7] M. Paul, K. Chiam, M. Cross, P. Fischer, H. Greenside, Pattern formation and dynamics in Rayleigh–Bénard convection: numerical simulations of experimentally realistic geometries, Physica D 184 (2003) 114–126.
[8] M. Cross, P. Hohenberg, Pattern formation outside of equilibrium, Rev. Mod. Phys. 65 (3) (1993) 851–1112.
[9] S. Chandrasekhar, Hydrodynamic and Hydromagnetic Stability, Oxford University Press, Oxford, 1961.
[10] P. Drazin, W. Reid, Hydrodynamic Stability, Cambridge University Press, Cambridge, 1981.
[11] E. Siggia, High Rayleigh number convection, Ann. Rev. Fluid Mech. 26 (1994) 137–168.
[12] S. Grossmann, D. Lohse, Scaling in thermal convection: a unifying theory, J. Fluid Mech. 407 (2000) 27–56.
[13] M. Hölling, H. Herwig, Asymptotic analysis of heat transfer in turbulent Rayleigh–Bénard convection, Int. J. Heat Mass Transfer 49 (2006) 1129–1136.
[14] J. Niemela, L. Skrbek, K. Sreenivasan, R. Donnelly, Turbulent convection at very high Rayleigh numbers, Nature 404 (2000) 837–840.
[15] X. Wu, A. Libchaber, Scaling relations in thermal turbulence: the aspect-ratio dependence, Phys. Rev. A 45 (1992) 842–845.
[16] A. Belmonte, A. Tilgner, A. Libchaber, Temperature and velocity boundary layers in turbulent convection, Phys. Rev. E 50 (1994) 269–278.
[17] S. Cioni, S. Ciliberto, J. Sommeria, Strongly turbulent Rayleigh–Bénard convection in mercury: comparison with results at moderate Prandtl number, J. Fluid Mech. 335 (1997) 111–140.
[18] R. Verzicco, R. Camussi, Transitional regimes of low-Prandtl thermal convection in a cylindrical cell, Phys. Fluids 9 (1997) 1287–1295.
[19] R. Verzicco, R. Camussi, Prandtl number effects in convective turbulence, J. Fluid Mech. 383 (1999) 55–73.
[20] V. Kek, U. Müller, Low Prandtl number convection in layers heated from below, Int. J. Heat Mass Transfer 36 (1993) 2795–2804.
[21] J. Glazier, T. Segawa, A. Naert, M. Sano, Evidence against 'ultrahard' thermal turbulence at very high Rayleigh numbers, Nature 398 (1999) 307–310.
[22] T. Takeshita, T. Segawa, J. Glazier, M. Sano, Thermal turbulence in mercury, Phys. Rev. Lett. 76 (1996) 1465–1468.
[23] R. Kerr, J. Herring, Prandtl number dependence of Nusselt number in direct numerical simulations, J. Fluid Mech. 419 (2000) 325–344.
[24] H. Rossby, A study of Bénard convection with and without rotation, J. Fluid Mech. 36 (1969) 309–335.
[25] R. Krishnamurthi, Some further studies on the transition to turbulent convection, J. Fluid Mech. 60 (1973) 285–303.
[26] R. Clever, F. Busse, Transition to time-dependent convection, J. Fluid Mech. 65 (1974) 625–645.
[27] R. Clever, F. Busse, Convection at very low Prandtl numbers, Phys. Fluids A 2 (1990) 334–339.
[28] M. Block, Surface tension as the cause of Bénard cells and surface deformation in a liquid film, Nature 178 (1956) 650–651.
[29] J. Pearson, On convection cells induced by surface tension, J. Fluid Mech. 4 (1958) 489–500.
[30] D. Nield, Surface tension and buoyancy effects in cellular convection, J. Fluid Mech. 19 (1964) 341–352.
[31] S. Davis, Thermocapillary instabilities, Ann. Rev. Fluid Mech. 19 (1987) 403–435.
[32] I. Hashim, S. Wilson, The onset of Bénard–Marangoni convection in a horizontal layer of fluid, Int. J. Eng. Sci. 37 (1999) 643–662.
[33] A. Thess, M. Bestehorn, Planform selection of in Bénard–Marangoni convection: l hexagons versus g hexagons, Phys. Rev. 52 (1995) 6358–6367.
[34] M. Proctor, Inertial convection at low Prandtl number, J. Fluid Mech. 82 (1977) 97–114.
[35] H. Ben Hadid, B. Roux, Buoyancy– and thermocapillary–driven flows in differentially heated cavities for low-Prandtl-number fluids, J. Fluid Mech. 235 (1992) 1–36.
[36] T. Boeck, Bénard–Marangoni convection at low Prandtl numbers, Ph.D. thesis, Technical University Ilmenau, Shaker-Verlag, Aachen, 2000.
[37] K. Eckert, M. Bestehorn, A. Thess, Square cells in surface-tension–driven Bénard convection: experiment and theory, J. Fluid Mech. 358 (1998) 149–197.
[38] J. Scheel, M. Cross, Scaling laws for rotating Rayleigh–Bénard convection, Phys. Rev. E 72 (5) (2005) 1–10.
[39] K. Julien, S. Legg, J. McWilliams, J. Werne, Hard turbulence in rotating Rayleigh–Bénard convection, Phys. Rev. E 53 (1996) R5557–R5560.
[40] J. Jou, K. Kung, C. Hsu, Effects of Coriolis force and surface tension on Bénard–Marangoni convective instability, Int. J. Heat Mass Transfer 40 (1997) 1447–1458.
[41] F. Chang, K. Chiang, Oscillatory instability analysis of Bénard–Marangoni convection in a rotating fluid under a uniform magnetic field, Int. J. Heat Mass Transfer 41 (1998) 2667–2675.
[42] J. Ristorcelli, J. Lumley, Instabilities, transition and turbulence in the Czochralski crystal melt, J. Cryst. Growth 116 (1992) 447–460.
[43] G. Müller, Convective instabilities in melt growth configurations, J. Cryst. Growth 128 (1993) 26–36.
[44] K. Kakimoto, Flow instability during crystal growth from the melt, Prog. Cryst. Growth Ch. 30 (1995) 191–215.
[45] K. Yi, K. Kakimoto, M. Eguchi, M. Watanabe, T. Shyo, T. Hibiya, Spoke patterns on molten silicon in Czochralski system, J. Cryst. Growth 144 (1994) 20–28.
[46] B. Basu, S. Enger, M. Breuer, F. Durst, Three-dimensional simulation of flow and thermal field in a Czochralski melt using a block-structured finite-volume method, J. Cryst. Growth 219 (2000) 123–143.
[47] A. Jones, An experimental model of the flow in Czochralski growth, J. Cryst. Growth 61 (1983) 235–244.
[48] M. Tanaka, M. Hasebe, N. Saito, Pattern transition of temperature distribution at Czochralski silicon melt surface, J. Cryst. Growth 180 (1997) 487–496.
[49] M. Watanabe, M. Eguchi, K. Kakimoto, T. Hibiya, Double-beam X-ray radiography system for three-dimensional flow visualization of molten silicon convection, J. Cryst. Growth 133 (1993) 23–28.
[50] O. Gräbner, G. Müller, J. Virbulis, E. Tomzig, Effects of various magnetic field configurations on temperature distributions in Czochralski silicon melts, Micro. Eng. 56 (2001) 83–88.
[51] S. Enger, Numerical simulation of flow and heat transfer in Czochralski crucibles, Ph.D. thesis, Lehrstuhl für Strömungsmechanik, Universität Erlangen-Nürnberg, 2001.
[52] M. Mihelčić, K. Wingerath, C. Pirron, Three-dimensional simulation of the Czochralski bulk flow, J. Cryst. Growth 69 (1984) 473–488.
[53] Q. Xiao, J. Derby, Three-dimensional melt flows in Czochralski oxide growth: high resolution, massively, parallel, finite element computations, J. Cryst. Growth 152 (1995) 169–182.

[54] S. Enger, O. Gräbner, G. Müller, M. Breuer, F. Durst, Comparison of measurements and numerical simulations of melt convection in Czochralski crystal growth of silicon, J. Cryst. Growth 230 (2001) 135–142.
[55] V. Kumar, B. Basu, S. Enger, G. Brenner, F. Durst, Role of Marangoni convection in Si–Czochralski melts – Part II: 3D predictions with crystal rotation, J. Cryst. Growth 255 (2003) 27–39.
[56] F. Schäfer, V. Kumar, M. Breuer, F. Durst, Visualization and computational steering of fluid motion in Czochralski crucibles during silicon crystal growth, Int. J. Comput. Fluid Dyn. 19 (7) (2005) 501–515.
[57] S. Enger, B. Basu, M. Breuer, F. Durst, Numerical study of three-dimensional mixed convection due to buoyancy and centrifugal force in an oxide melt for Czochralski growth, J. Cryst. Growth 219 (2000) 144–164.
[58] B. Basu, S. Enger, M. Breuer, F. Durst, Effect of crystal rotation on the three-dimensional mixed convection in the oxide melt for Czochralski growth, J. Cryst. Growth 230 (2001) 148–154.
[59] D. Vizman, O. Gräbner, G. Müller, Three-dimensional numerical simulation of thermal convection in an industrial Czochralski melt: comparison to experimental results, J. Cryst. Growth 233 (2001) 687–698.
[60] V. Kumar, B. Basu, S. Enger, G. Brenner, F. Durst, Role of Marangoni convection in Si–Czochralski melts – Part I: 3D predictions without crystal, J. Cryst. Growth 253 (2003) 142–154.
[61] Y. Kishida, K. Okazawa, Geostrophic turbulence in CZ silicon crucible, J. Cryst. Growth 198/199 (1999) 135–140.
[62] Y. Kishida, T. Tamaki, K. Okazawa, W. Ohashi, Geostrophic turbulence in CZ silicon melt under CUSP magnetic field, J. Cryst. Growth 273 (2005) 329–339.
[63] M. Watanabe, D. Vizman, J. Friedrich, G. Müller, Large modification of crystal–melt interface shape during Si crystal growth by using electromagnetic Czochralski method (EMCZ), J. Cryst. Growth 292 (2006) 252–256.
[64] C. Wagner, Turbulente Transportvorgänge in idealisierten Czochralski–Kristallzüchtungsanordnungen, Habilitationsschrift, Lehrstuhl für Fluidmechanik, Technische Universität München, 2003.
[65] C. Wagner, R. Friedrich, Direct numerical simulation of momentum and heat transport in idealized Czochralski crystal growth configurations, Int. J. Heat Fluid Flow 25 (2004) 431–443.
[66] A. Raufeisen, T. Botsch, E. Franz, V. Kumar, M. Breuer, F. Durst, Prediction of flow and heat transfer in a Czochralski crucible using LES with interface tracking, in: Oberlack Guenther, Weller Khujadze, Osman Frewer, Peinke (Eds.), Progress in Turbulence, 2, Springer-Verlag, Berlin, Heidelberg, New York, 2007.
[67] A. Raufeisen, T. Botsch, E. Franz, V. Kumar, M. Breuer, F. Durst, Large eddy simulation of flow and heat transfer with interface prediction in a Czochralski configuration for crystal growth, Euromech Colloquium, 469, Dresden, Germany, 2005.
[68] M. Breuer, W. Rodi, Large-eddy simulation of complex turbulent flows of practical interest, in: E. Hirschel (Ed.), Flow Simulation with High-Performance Computers II, Notes on Numer. Fluid Mech, vol. 52, Vieweg-Verlag, Braunschweig, 1996, pp. 258–274.
[69] M. Breuer, Large eddy simulation of the sub-critical flow past a circular cylinder: numerical and modeling aspects, Int. J. Numer. Meth. Fluids 28 (1998) 1281–1302.
[70] M. Breuer, A challenging test case for large eddy simulation: high Reynolds number circular cylinder flow, Int. J. Heat Fluid Flow 21 (5) (2000) 648–654.
[71] M. Breuer, Direkte Numerische Simulation und Large-Eddy Simulation turbulenter Strömungen auf Hochleistungsrechnern, Habilitationsschrift, Universität Erlangen–Nürnberg, Berichte aus der Strömungstechnik, ISBN 3-8265-9958-6, Shaker-Verlag, Aachen, 2002.
[72] J. Ferziger, M. Perić, Computational Methods for Fluid Dynamics, third ed., Springer-Verlag, 2002.
[73] H.L. Stone, Iterative solution of implicit approximations of multidimensional partial differential equations, SIAM J. Numer. Anal. 5 (530–558) (1968) 530–558.
[74] C. Rhie, W. Chow, A numerical study of the turbulent flow past an isolated airfoil with trailing edge separation, AIAA J. 21 (1983) 1525–1532.
[75] A. Kolmogorov, The local structure of turbulence in an incompressible fluid at very high reynolds numbers, Dokl. Akad. Nauk SSSR 30 (1941) 299–303.
[76] A. Kolmogorov, Dissipation of energy in the locally isotropic turbulence, Dokl. Akad. Nauk SSSR 32 (1941) 16–18.
[77] S. Pope, Turbulent Flows, Cambridge University Press, 2000.
[78] G. Grötzbach, Spatial resolution requirements for direct numerical simulation of the Rayleigh–Bénard convection, J. Comput. Phys. 49 (1983) 241–264.
[79] J. Fein, R. Pfeffer, An experimental study of the effects of Prandtl number on thermal convection in a rotating, differentially heated cylindrical annulus of fluids, J. Fluid Mech. 75 (1976) 81–112.
[80] K. Kakimoto, M. Watanabe, M. Eguchi, T. Hibiya, The baroclinic flow instability in rotating silicon melt, J. Cryst. Growth 128 (1993) 288–292.
[81] R. Hide, W. Fowlis, Thermal convection in a rotating annulus of liquid: effect of viscosity on the transition between axisymmetric and non-axisymmetric flow regimes, J. Atmospher. Sci. 22 (1965) 541–558.
[82] A. Jones, The temperature field of a model Czochralski melt, J. Cryst. Growth 69 (1984) 165–172.
[83] V. Kumar, G. Biswas, G. Brenner, F. Durst, Effect of thermocapillary convection in an industrial Czochralski crucible: numerical simulation, Int. J. Heat Mass Transfer 46 (2003) 1641–1652.